Velocity field, surface profile and curvature resolution of steep and short free-surface waves

Matthieu A. André · Philippe M. Bardet

Abstract On steep, millimeter-scale, 2D water waves, surface profile, and subsurface velocity field are measured with high-spatio-temporal resolution. This allows resolving surface vorticity, which is captured in the surface boundary layer and compared with its direct computation from interface curvature and velocity. Data are obtained with a combination of high-magnification time-resolved particle image velocimetry (PIV) and planar laser-induced fluorescence. The latter is used to resolve the surface profile and serves as a processing mask for the former. PIV processing schemes are compared to optimize accuracy locally, and profilometry data are treated to obtain surface curvature. This diagnostic enables new insights into free-surface dynamic, in particular, wave growth and surface vorticity generation, for flow regimes not studied previously. The technique is demonstrated on a high-speed water jet discharging in quiescent air at a Reynolds number of 4.8×10^4. Shear-layer instability below the surface leads to streamwise traveling waves with wavelength $\lambda \sim$ 2 mm and steepness $2\pi a/\lambda \geq 2.0$, where a is the crest to trough amplitude. Flow structures are resolved at these scales by recording at 16 kHz with a magnification of 4.

1 Introduction

Particle image velocimetry (PIV) has become the de facto diagnostics for measuring fluid velocity fields (Raffel et al.

1998; Adrian and Westerweel 2011). It has been successfully applied to both liquid and gas flows. Recent advances in technology and techniques have enabled the study of small-scale flows (μ-PIV, Meinhart et al. 1999; Santiago et al. 1998) as well as high-speed flows in a time-resolved manner (Supersonic PIV, Bryanston-Cross and Epstein 1990; Bitter et al. 2011). PIV technique has been extended to measure the three components of velocity in planes [Stereoscopic PIV, see review by Prasad (2000)] or in volumes (Tomographic PIV, Elsinga et al. 2006 or Holographic PIV, Barnhart et al. 1994). The main limitations to PIV uncertainty and performance are given by the dynamic velocity and spatial ranges (Adrian 1997). Various methods exist for increasing these ranges that include multiple exposures and multiple fields of view (Adrian 1988).

For multiphase flows and fluid structure interactions, challenges arise in the identification of the phases, and in the PIV processing in the vicinity of the interface. Commonly, the unwanted phase is masked on the raw images prior to processing. For rigid objects with known geometry and motion (such as wall, turbine blade, etc.), the mask can be defined a priori. However, for compliant interfaces, the mask must be determined on each frame using the raw PIV images or with additional measurements. In liquid–solid or liquid–liquid interfaces, the two phases are usually selected such that they have similar refractive indices and do not obstruct optical access (Wiederseiner et al. 2011). For example, Westerweel et al. (2002) used a dye tagging technique associated with index matching for identifying phases in a liquid–liquid flow.

Gases typically have very low refractive indices and such techniques are not applicable to liquid–gas interfaces. Most studies of free-surface flows with low level of surface deformations have made use of a single camera and relied

M. A. André (✉) · P. M. Bardet
Department of Mechanical and Aerospace Engineering, The
George Washington University, Washington, DC, USA
e-mail: matandre@gwu.edu

P. M. Bardet
e-mail: bardet@gwu.edu

on light being partially reflected by the surface when imaged from below. The interface is found using reflection and/or change in background intensity (Dabiri and Gharib 1997; Peirson 1997; Foeth et al. 2006; Qiao and Duncan 2001; Li et al. 2005; Hirsa et al. 2001; Perlin et al. 1996) or by taking advantage of the Brewster angle (Kuang-An and Liu 1998; Lin and Perlin 1998). Dabiri and Gharib (2001) measured surface deformations using the reflection of a colormap by the surface. For higher surface deformations, the particle images reflected by the surface are not present anymore and a second view must be used to identify the surface profile. Siddiqui et al. (2001) recorded the surface location with a dedicated top down view camera in centimeter scale wind induced micro-breakers. Law et al. (1999) used a split-screen technique to gain access to the velocity field and surface profile in a submerged turbulent jet. Belden and Techet (2011) performed PIV in both phases of a breaking gravity wave with one camera and one laser per phase. The lasers had different wavelengths, and the phases were isolated spectrally. Available data are for waves with limited steepness, and no high resolution velocity fields are available below steep millimeter-scale waves. Data near an interface are invaluable for understanding interfacial mechanisms. For example, shear stress can transport momentum across an interface.

PIV processing near an interface requires special treatment to cope with the mask intersecting the PIV domain. Refined schemes have been developed for measuring velocity and shear near an interface primarily for flat or slightly disturbed interfaces (Phan et al. 2005; Theunissen et al. 2008; Lin and Rockwell 1995). Special processing techniques, such as multigrid and window deformation, increase the spatial resolution and improve the measurement of shear (Scarano and Riethmuller 2000). The correlation method [image or Fast Fourier Transform (FFT)] usually includes only the non-masked area, but a mirrored image can be added in the masked area to treat high deformations (Tsuei and Savaş 2000).

In the case of an unsteady 2D shear-free surface, surface parallel vorticity (i.e., out of plane vorticity) is given by Eq. 1 (Batchelor 1967; Longuet-Higgins 1992; Lundgren and Koumoutsakos 1999; Saffman 1993; Lugt 1987).

$$\omega_{n=0} = 2\mathbf{s} \cdot \nabla \mathbf{u} \cdot \mathbf{n} \tag{1}$$

In this equation, tangent and normal unit vectors to the surface ($\mathbf{s}$, $\mathbf{n}$) are defined following a curvilinear coordinate system shown in Fig. 1.

The surface vorticity is present in a viscous boundary layer, where the depth is on the order of Stokes layer (Longuet-Higgins 1992). To the authors' knowledge, no experiment has been able to directly measure surface vorticity using Eq. 1. Banner and Peirson (1998) developed a high resolution PIV system to capture tangential stress
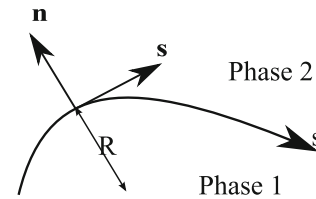

Fig. 1 Curvilinar coordinate system. $\mathbf{s}$ and $\mathbf{n}$ are the vectors tangent and normal to the surface, respectively. s is the curvilinear coordinate along the surface. R is the local radius of curvature

below wind driven gravity waves populated with parasitic capillaries. Their 300 μm spatial resolution allowed capturing the shear stress of small curvature gravity waves but was insufficient in the trough of capillary waves. The strong vorticity there contaminated the measurement of shear.

Among others, Lin and Perlin (1998, 2001), Peirson (1997), Lin and Rockwell (1995), and Gharib and Weigand (1996) have been able to resolve vorticity field close to a free surface and quantify some of the vorticity that has viscously diffused into the flow, but no results were reported that compared measured vorticity with results of Eq. 1.

Additionally, the surface parallel vorticity flux (Eq. 2) can also be computed (Rood 1995; Gharib and Weigand 1996).

$$\nu \mathbf{n} \cdot \nabla \omega = \mathbf{n} \times \left[\frac{\partial \mathbf{u}}{\partial t} + \mathbf{u} \cdot \nabla \mathbf{u} + \frac{\nabla p}{\rho} - \mathbf{g} \right] \tag{2}$$

For a deformed free surface, Eqs. 1 and 2 require knowledge of the surface curvature, κ. Surface curvature involves the second derivative of the surface profile and is challenging to compute from experimental data.

This is also testing for interface tracking schemes implemented in computational fluid dynamics (CFD), where the curvature must be known in order to compute the surface tension force. Furthermore, during coalescence and breakup events, when interfaces reconnect or disconnect, curvature diverges, which can lead to numerical instabilities. Various methods have been proposed for increasing the accuracy of curvature calculation (François et al. 2006; Scardovelli and Zaleski 1999). Similar difficulties are also encountered in computer vision (Flynn and Jain 1989). Resolving the vorticity flux is beneficial to understanding the interaction of vortical structures with a surface. For instance, vorticity can flux out of the liquid, such as at an accelerating free surface (Gharib and Weigand 1996), or can flux inside the flow in the opposite case (Dabiri and Gharib 1997). Injection of vorticity can increase mixing and heat and mass interphase transfers through surface renewal. For steep waves, vorticity flux is linked to flow separation (Longuet-Higgins 1992, 1994) and can strongly

influence evolution of spilling breakers (Qiao and Duncan 2001; Duncan et al. 1999).

In this paper, PLIF and PIV are combined to resolve the surface profile and the velocity field below a highly deformed free surface. The small time- and length-scales of the flow under study require a high-spatio-temporal resolution diagnostic, which is presented in the first section. Identification and treatment of the free surface are then described. Several PIV processing schemes are assessed to improve the accuracy near the interface.

Post-processing of velocity and surface profile data at the interface allows for the direct measurement of surface vorticity, which can be compared with PIV data that are resolved in the viscous layer. Sample velocity fields with evidence of surface vorticity generation are presented and compared with analytical results of (Longuet-Higgins 1992; Brennen 1970).

2 Experiment

The experimental technique is demonstrated on a high-speed water jet, where the surface is populated with steep, 2D millimeter-scale waves above strong spanwise vortices.

2.1 Apparatus

In this experiment, a rectangular water jet flows onto an open-top clear acrylic channel. In this configuration, initially quiescent air is freely accelerated by the moving liquid.

A two-dimensional (2D) symmetric contoured nozzle, designed to minimize laminar boundary layer thickness and prevent the formation of Görtler vortices, generates a uniform top-hat slab jet with bulk velocity U adjustable between 1 and 10 m s^{-1}. The jet thickness, t_{jet}, is 20.3 mm and the width, w_{jet}, is 146.0 mm. This corresponds to Reynolds numbers ranging from $Re = Ut_{jet}/\nu = 2.0 \times 10^4$ to 2.0×10^5 based on the jet thickness, and $Re_\theta = U\theta/\nu =$ 100–300 based on the boundary layer momentum thickness, θ. The boundary layer thickness is less than 10 % of the jet thickness for the lowest Reynolds number studied here, which allows for neglecting the effects of the bottom and side walls on the free surface. Flat extension plates of various lengths can be fitted to the nozzle exit in order to vary Re_θ for a given U. The reader can refer to André and Bardet (2012) for more details on the apparatus and characterization of the jet.

The top laminar boundary layer that develops along the upper nozzle wall undergoes a relaxation at the exit of the nozzle that is due to a change in boundary condition from no-slip to shear free. Depending on Re_θ this shear layer

below the surface can be unstable and roll up into 2D spanwise vortices.

Brennen (1970) predicted with linear stability analysis that the dimensionless frequency of the instability, $\bar{f}$, given by Eq. 3 where f is the instability frequency, tends toward 0.175 in the inviscid limit.

$$\bar{f} = \frac{2\pi f\theta}{U} \tag{3}$$

In the present study, the disturbances have millimeter-scale wavelengths and the wave steepness parameter ak (amplitude × wavenumber) can be up to 2. Here the amplitude is the height from trough to crest, which is twice the amplitude defined in analytical work, such as Longuet-Higgins (1992, 1994).

Following Yu and Tryggvason (1990), it is appropriate to express the Reynolds, Weber, and Froude numbers based on the circulation per wavelength in the shear layer Γ. In the present work, $Re_\Gamma = \Gamma/\nu = 5 \times 10^3$ (note that Re_Γ is initially directly proportional to Re_θ when using Brennen's relation between θ and λ), $We_\Gamma = \rho\Gamma^2/\sigma\lambda = 1.7 \times 10^2$ (σ is the surface tension) and $Fr_\Gamma = \Gamma^2/\sqrt{\rho g\lambda} = 18$. These parameters indicate that the flow is dominated by inertia over viscous, surface tension, and gravity forces, respectively.

2.2 Instrumentation

Figure 2 shows the layout of the experimental setup. PIV is performed in the liquid in the direct vicinity of the free surface. Table 1 presents the details of the PIV setup.

The laser beam is shaped into a light sheet aligned in the streamwise direction, x, and normal to the mean free surface. The sheet is 40 mm wide, and its thickness w has been calculated (Crimaldi 2008) to be 0.2 mm at the beam waist (which is located at the intersection with the surface).

The PIV camera is angled up from the horizontal plane to avoid the meniscus and surface deformations in the foreground of the working plane. The effective viewing angle when taking into account refraction at the channel side wall is $\beta = \arcsin(n_{air} \sin \alpha_1/n_{water}) = 8.8°$. Perspective effects due to this angle are corrected in a calibration phase described hereafter.

To process the PIV images, the location of the free surface must be known a priori. However, this is not readily detectable on the raw images alone due to partial reflection and distortion as illustrated in Fig. 3. Hence, PLIF is performed to identify the interface with a second camera that points down at $\alpha_2 = 28.0°$ above the surface. The water is homogeneously dyed with rhodamine 6G. The fluorescent dye is excited with the same laser sheet as for PIV, which ensures intrinsic alignment between PIV and PLIF planes.
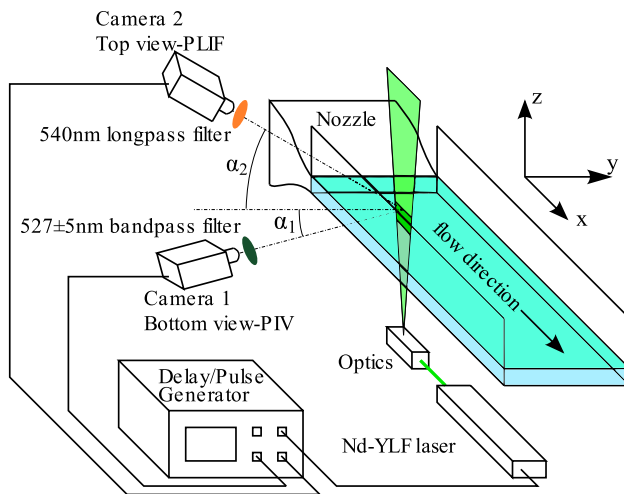
Fig. 2 Diagram of the experimental setup

Table 1 Experimental equipment and parameters

Equipment or parameters	PIV	PLIF
Tracer	2-μm Silver-coated hollow glass spheres	Rhodamine 6G
Light source	Nd:YLF 527 nm, 4 mJ per pulse at 16 kHz	Same as PIV
Camera	Phantom V710	Phantom V311
Objective	Nikon 105 mm + bellows	Nikon 60 mm + 2× teleconverter + bellows
Field of view	4 × 2.5 mm²	7.5 × 4.3 mm²
Resolution	800 × 504 pixels	800 × 456 pixels
Magnification	4.11	2.13
Camera inclination	$\alpha_1 = 11.7°$ upward	$\alpha_2 = 28.0°$ downward
Recording rate	16,000 fps	8,000 fps

Fig. 3 PIV image with a deformed free surface. Contrast has been enhanced. The interface cannot be directly and accurately found because of the distorted reflections and refractions. An internally reflected beam can be seen on the *left* of the image

The interface location is then extracted and provides a mask for the PIV processing. Both cameras are calibrated with a single target (Applied Image Inc. 0.200 mm pitch square grid) that is held at the same location for each view. This ensures an accurate correspondence of the top and bottom views. Three parallel planes are acquired to take into account the depth of field of each camera. The mapping function between raw and corrected images is generated in the calibration process using the software DaVis 8.1. from LaVision, Inc. It fits a third order polynomial mapping function.

Cameras and laser are synchronized with a delay/pulse generator (Berkeley Nucleonics 575, 250 ps resolution). Each camera is fitted with a macro lens on a bellows. Details are given in Table 1 for the data reported in Figs. 18 and 20. These configurations offer high magnification ($M = 2$–4) with a sufficient working distance (5–15 cm). The depth of field is small (1.25 mm at $M = 3$ and f/5.6), but it is still larger than the laser sheet thickness. Ad hoc spectral filters are added to isolate the respective signals. A 527 ± 5 nm bandpass filter collects the light reflected by the particles alone for PIV imaging, while a 540 nm long-pass filter isolates the light fluoresced by the dye for PLIF imaging.

PIV and PLIF are well suited for the study of 2D flows like the one presented here. The surface has been observed with a pulsed light and camera and appears 2D during the shear-layer relaxation and growth of the disturbances.

2.3 Data acquisition

The recording stations along the x direction are located from 3 mm upstream to 80 mm downstream of the nozzle exit ($x = 0$). The laser sheet is parallel to the side wall and located 25 mm away from it, due to restrictions on the working distance. However, the imaging plane is far enough from the side wall that the latter has no effect on the measurement stations that close to the nozzle exit: in this supercritical flow, the wake from the side wall forms an angle of 18° for the lowest Re data reported here and closes 45 cm downstream (Henderson 1996).

Table 1 summarizes the recording parameters. The recording rate results from a trade-off between spatial and temporal resolutions of the cameras as well as laser pulse energy. The pulses separation is monitored with a high-speed photodiode. Because high repetition rate lasers, particularly Nd-YLF lasers, have long build up time between the cavity Q-switching and the actual pulse, significant timing errors can occur if not monitored and corrected for (Bardet et al. 2013). The PLIF camera is operated at half the frame rate of PIV, because of the lower available frame rate. The change in the surface profile between two consecutive PLIF images is negligibly small, and a 16 kHz sequence is generated artificially by a translation of the 8 kHz raw sequence. Profilometry

calculations are based on the 8 kHz sequence in order to avoid oversampling.

The PLIF field of view is larger than for PIV in order to ensure that the mask will cover the whole PIV frame. The field of view is only a fraction of the laser sheet width, which ensures a good uniformity of the illumination intensity over the image.

3 Data processing

A two-step processing algorithm is presented to identify the interface in the PLIF data. Several PIV processing schemes near the interface are evaluated. Their accuracy is estimated using synthetic images.

3.1 PLIF processing

The PLIF images are processed with MATLAB R2011b to extract masks for the PIV images.

3.1.1 Surface profile

For the high-magnification setup employed here, the thickness of the laser sheet is noticeable on the PLIF images. The interface appears as a gradually varying intensity region as explained in Fig. 4. Figure 5 shows an example of an intensity profile along a line crossing the interface perpendicularly. Above pixel 210, there is
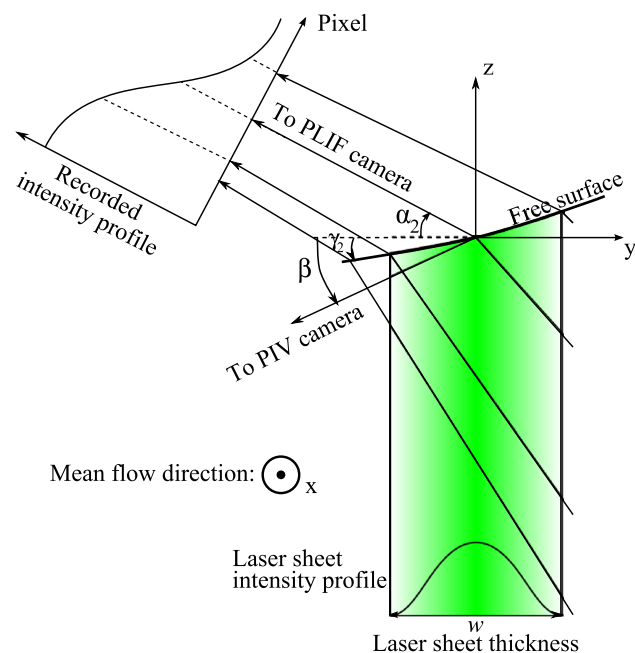
Fig. 4 Effect of the laser sheet thickness and surface spanwise angle on the image intensity profile across the interface. Details of the intensity profile is shown in Fig. 5
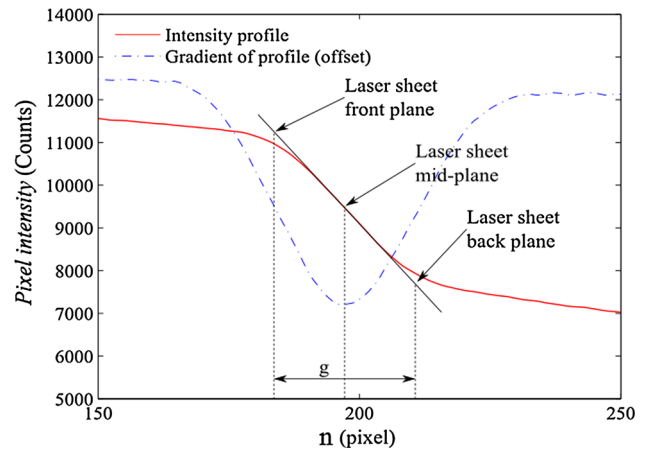
Fig. 5 Intensity plot for a line crossing the interface in a PLIF image. The surface normal coordinate n is defined in Figs. 1 and 7. *Pixel* intensity is above 2^{12} because raw data (12-bit) are exported as 16-bit images

background noise caused by out of plane fluorescence due to scattered light. Below pixel 185, the increase in intensity is due to longer paths of laser light in the illuminated section as illustrated in Fig. 4. The gradient zone in the middle bridges the gap. Here, one takes advantage of this to detect the surface location.

Because the water-air interface is a semi-reflective mirror, traditional edge detection cannot be employed. Depending on the incidence angle of the laser light with respect to the surface and, hence the local slope of the surface (Fresnel's equations), a fraction to all of the laser light can be reflected into the liquid. For waves with streamwise slope below Brewster's angle (41.7° for water–air interface), a small fraction of the initial laser sheet (∼0–10 %) is reflected in the liquid. This is negligible, and hence, the surface does not affect the local PIV resolution. Above this angle, the reflectance increases sharply, and above the water-air critical angle (48.6°) total internal reflection occurs, resulting in the laser light being entirely reflected in the liquid phase. Furthermore, for these steep waves, the streamwise concave curvature of the waves results in the reflected light being focused to beamlets. These secondary beamlets are visible on both PLIF and PIV raw images, see Figs. 3 and 6, respectively. Beamlets can be reflected several times as in Fig. 6 where the beamlet is redirected in the bulk. Because of the 2D nature of the surface, reflections are close to the focal plane and few particles outside of the investigation plane are illuminated. Thus, the beamlets will not result in spurious data as could be encountered for highly three dimensional free surfaces (Bardet et al. 2010). However, they will decrease the local signal to noise ratio (SNR) of the raw PIV images of waves with slopes greater than the Brewster's angle. In the present case, this was found to not significantly affect
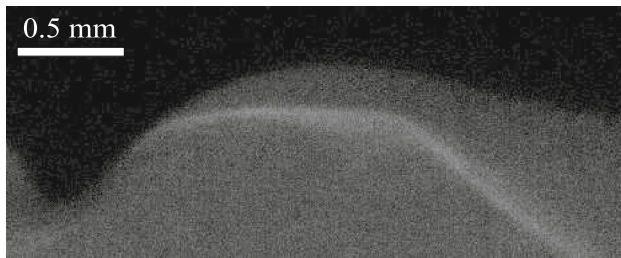
Fig. 6 Example of PLIF image where a beamlet from "steep" left wavefront is internally reflected twice. *Note* this frame does not correspond to PIV frame of Fig. 3
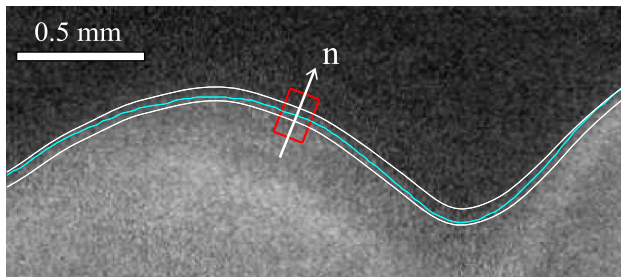

Fig. 7 Illustration of PLIF image processing. The initial surface detection (Otsu's method) is plotted in *cyan* and an example of interrogation window used for the second step of the surface detection is shown in *red*. The calculated back and front planes of the laser sheet are plotted in *white*. The *mid-plane line* is not plotted for clarity

Fig. 8 Iso-contours of the normalized gradient zone thickness g/w versus streamwise and spanwise surface angles for α_2 of the present setup. The *dark gray area* below the curve $g/w = 0$ corresponds to the slopes that are theoretically not measurable. In practice, the foreground flow may mask the analysis plane and the light sheet cannot directly illuminate the surface when $|\gamma_1| > 90°$, which is marked in *light gray*

the velocity field results as illustrated in Sect. 5. These reflections create locally large intensity gradients in the PLIF images, which make direct edge detection schemes such as Sobel or Canny edge detectors not robust enough. Hence, extraction of surface profile from PLIF images is processed in two steps.

The image is first smoothed with a 5×5 Gaussian filter and segmented with Otsu's method (1975). This method minimizes the intraclass variance (of bright and dark based on the intensity histogram), which ensures the image is approximately segmented half way between the dark region above the surface and the light region below the surface. This produces a preliminary coarse and robust estimation of the free-surface location (cyan line in Fig. 7). In particular, this scheme is fairly insensitive to beamlets created by internal reflections because these bright pixels are in minority in the image histogram.

In a second step, interrogation windows 20 pixels wide by 30 pixels high are defined. This size allows for a good resolution of the interface and the capturing of the gradient zone, which is usually between 5 and 20 pixels wide depending on the surface angle and the magnification. The windows are centered on the previously estimated interface location and oriented normal to it. An example of such an interrogation window is shown in red in Fig. 7. Each window is averaged along the surface tangent direction,
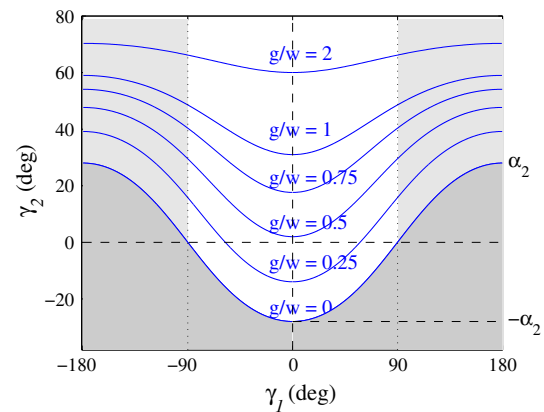
producing a 1D intensity profile such as that shown in Fig. 5. The 1D gradient is computed to find the location of the inflexion point. The mid-plane location is reconstructed using these interrogation windows with an overlap of 75 %. The interface is projected on the PIV images, and masks are generated for each PIV sample.

Additionally, the width of this measured gradient zone, g defined in Fig. 5, can be measured to gain access to the location of the back and front planes of the laser sheet. This depends on the streamwise and spanwise angles of the surface, γ_1 and γ_2, respectively. For a given α_2, γ_1, and g/w, there is only one possible value of γ_2 in the range $[-180°, 180°]$, Fig. 8. See "Appendix 1" for the derivation of the equations leading to this solution. $g/w = 0$ corresponds to a surface normal vector perpendicular to the optical axis of imaging. The dark gray area corresponds to $g/w < 0$, meaning that the interface is not optically accessible. The light gray region marks $|\gamma_1| > 90°$ where the laser sheet cannot illuminate the interface without internal reflections. These cannot be reliably captured with the current method, although such waves are sometimes visible, but not reported here. Streamwise angles >90° could be reliably measured by inclining the laser sheet and the camera toward the steepest (downstream) part of the wave; however, the angle measuring range would be reduced on the upstream side of the wave.

γ_1 is readily accessible from the data and for a given g/w, γ_2 can be found graphically using Fig. 8 or by solving Eq. 20. This model assumes that the viewing angle is constant. In the present case, the field of view is small (7.5 mm) compared to the working distance (50 mm), and the viewing angle varies by a maximum of $\pm 1°$ vertically and

±4° horizontally. This could be corrected with a pinhole camera model.

To the first order, the laser sheet mid-plane is at the location of maximum gradient of the intensity profile. This holds true for any symmetrical light distribution. The present laser has a symmetric bell-like profile (manufacturer data). The value of the maximum gradient is proportional to g/w, and the coefficient of proportionality is determined by calibration in the case of a flat free surface, which is observable for $Re_\theta < 150$. The spanwise angle of the free surface can be calculated with Eq. 20, although this is not used any further in the present study due to the 2D nature of the flow. Front and back planes location of the laser sheet are reported in Fig. 7.

3.1.2 Uncertainty on surface location

The two-step method for identifying the free surface in the PLIF images has an estimated uncertainty of ±2 pixels or ±0.01 mm. Horizontal averaging over 20 pixels in the second step of the processing is the main contributor as the profile in each interrogation windows is flat within ±2 pixels. Nevertheless, in the sharpest troughs, the deviation can be larger, resulting in a reduced accuracy and smoothing of the sharper troughs. An adaptive window size based on the local streamwise curvature could improve the results but has not been deemed necessary. The calibration has a negligible error of 0.17 pixel or 0.0006 mm for the PLIF images.

The spanwise surface curvature κ_y will affect the measurement of the surface location. κ_y has a second order effect in the expression of the surface profile as shown in "Appendix 2".

For the 2D flow studied here γ_2 and κ_y are small, and an error in surface elevation of 5 % of the sheet thickness, or 0.009 mm, represents a conservative estimate. Therefore, the combined accuracy on the surface elevation at the mid-laser-sheet plane is ±0.013 mm, or within 7 % of the laser sheet thickness.

3.2 PIV processing

3.2.1 PIV algorithm

The PIV sequence is processed with Davis 8.1. from La-Vision, Inc. The PIV processing consists of a multipass FFT cross-correlation scheme with decreasing interrogation window size. The mean displacement of the particles between consecutive frames is 20–30 pixels in the bulk and down to about 12 pixels at the surface; this is correctly captured by an initial 64 × 64 pixels interrogation window. This size is then progressively decreased down to 24 × 24 pixels, with 50 % overlap and Gaussian windowing.

Table 2 PIV processing schemes near the surface

Scheme	Correlation method	Pixels used
A	FFT	Non-masked only
B	FFT	All
C	Direct from image	Non-masked only

Outliers are removed between passes based on the difference with the neighboring vectors. During the last pass, the interrogation window is deformed to minimize peak locking and increase correlation coefficients. The raw image is mapped according to the local velocity field using a Lanczos reconstruction (Duchon 1979). The final vector field is smoothed with a 3 × 3 Gaussian filter to improve the computation of derivatives such as vorticity.

Similar parameters apply to the windows intersecting the edge of the mask. For these windows, however, three types of processing, described in Table 2, have been evaluated in order to increase the accuracy near the interface. The schemes A and B use cross correlation based on FFT of the interrogation window. Scheme A sets the pixels lying outside the mask to zero, while scheme B includes them in the calculation. Scheme C is a direct image correlation using only the pixels lying inside the mask. In all three schemes, a vector is calculated only if the center of the interrogation window lies inside the mask.

To select the best processing scheme for the edge of the mask and assess its accuracy, the three schemes are tested on synthetic PIV images of a Lamb–Oseen vortex (Saffman 1993) having similar characteristics to those observed in the flow. An arbitrary mask is applied, and the image is mirrored about the interface to model reflections at the free surface. Note that the shear-free condition is not satisfied at the interface. It can be argued that this will lead to a conservative estimate of the error since PIV accuracy is known to decrease in the presence of shear. The latter decreases the correlation peak signal to noise ratio (Scarano and Riethmuller 2000; Adrian and Westerweel 2011).

Various vortex locations and sizes have been evaluated, shown in Fig. 9; however, only a summary of the results is presented for sake of conciseness.

Firstly, a significant error was observed in regions of high vorticity when a bilinear image reconstruction was used. These errors were canceled using a slightly more computationally intensive Lanczos reconstruction. Figure 10 presents a comparison of the error in vorticity for the case C2 with a bilinear reconstruction on the left, and a Lanczos reconstruction on the right. Error maps have been averaged over 6 randomly generated pairs of synthetic images to obtain second order statistics.

When a large vortex intersects the surface, such as in the cases T2, M2, and C2 (see Fig. 9), the error in vorticity for the windows close to the surface is large, up to 23.5 % for the case C2 shown on the right of Fig. 10. Error on the vorticity measured away from the surface is uniform, at about 3.9 %. For a smaller vortex, where the core is below the surface (cases T1, M1, and C1), the vorticity RMS error near the surface is 6.2 %.

Overall, the RMS error for the windows non-adjacent to the surface (bulk of the flow) is 1.8 % for the velocity and 3.9 % for the vorticity. The error in surface velocity is 2.9 %. The error in surface vorticity is larger than in the bulk, partly because one or two neighboring velocity vectors are missing when computing the vorticity. In these cases, the
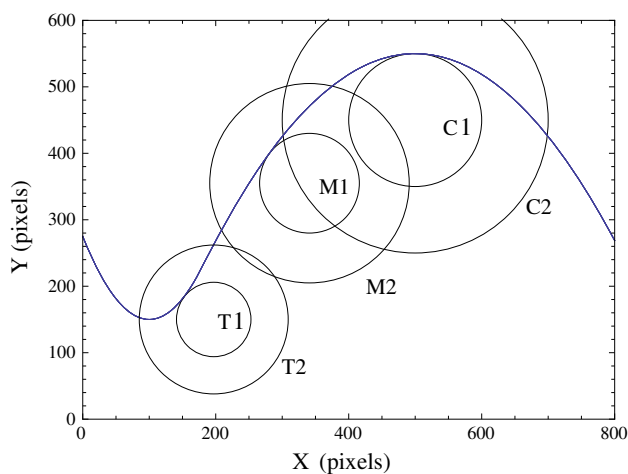
central difference scheme is replaced by a less accurate backward difference during the computation of vorticity.

The processing scheme A has been chosen for its better accuracy and computational efficiency. Scheme C is too computationally expensive with limited benefits after post-processing. Scheme B is also avoided because it relies mostly on post-processing. This comparative study also shows that the error in near-surface vorticity for the synthetic data is at least 6.2 % in low vorticity regions and can reach up to 25 % in high vorticity regions.

3.2.2 PIV spatial uncertainty

Due to the effective viewing angle β of the PIV camera, interrogation windows are 2D projections of parallelepiped. Hence for 2D flows, the resulting velocity will be calculated from a projected area that is actually larger than the orthogonal projection of the interrogation window on the light sheet, Fig. 11. As a result, the flow field will be vertically smoothed.

Here, the light rays from each interrogation window can be considered parallel, because the window size ($D = 0.117$ mm) is small compared to the working distance (~ 50 mm). Interrogation window overlap helps obtain a smoother and denser velocity field. Prior to computing the FFT, interrogation regions typically have Gaussian windowing applied to them to minimize leakage. In the case considered here, where the flow can be assumed 2D, a window of height D will encompass a larger projected height of the flow; it is given by $D' = D + w \sin(\beta)$. Therefore, in this configuration, interrogation windows are equivalent to a vertical trapezoidal weighting function, Fig. 11. Furthermore, the particle intensity distribution is
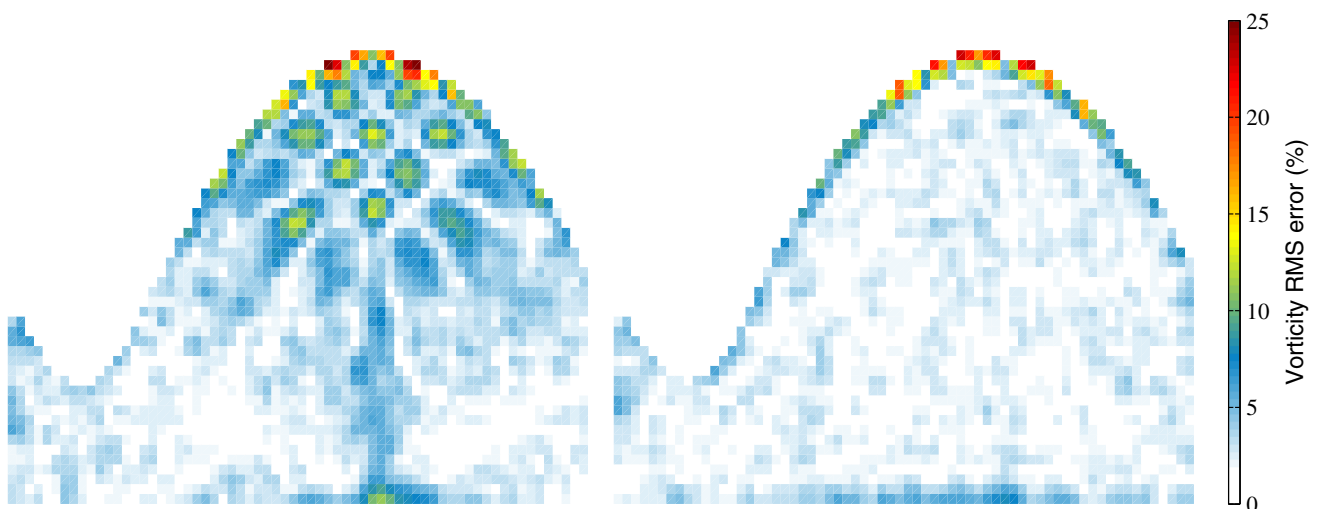

Fig. 9 Map of the synthetic vortices studied. The vortex core is plotted for each case. Interface is the *blue line*

Fig. 10 Vorticity RMS error maps of synthetic case C2 processed with scheme A. A bilinear image reconstruction has been used on the *left* sub-figure, a Lanczos reconstruction on the *right*. Large error is visible in the bulk in region of high vorticity for the bilinear reconstruction. The vorticity error for the windows adjacent to the interface is comparable
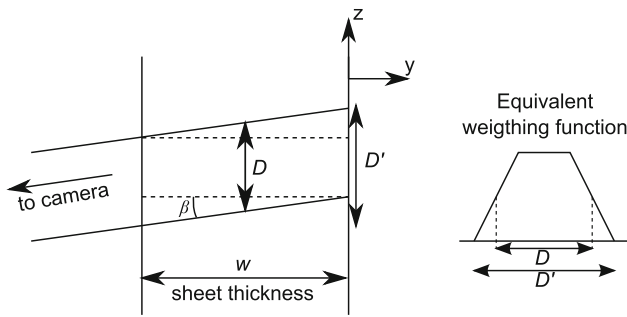
Fig. 11 Effect of the sheet thickness and camera angle on the interrogation window for a 2D flow. Angle is exaggerated for better visualization

weighted along the y direction by the laser sheet intensity profile, typically close to a Gaussian. The resulting interrogation window in the vertical direction is the convolution of these two functions. A Gaussian convoluted with a trapezoid retains a bell-like shape. Therefore, the effects of the angle and sheet thickness introduce limited distortions on the results. In the present case, with $D = 0.117$ mm, $w = 0.2$ and $\beta = 8.8°$, the overall projected size of the interrogation window becomes $D' = 0.144$ mm. For a 0.117 mm interrogation window and an overlap of 50 %, a vector will be displayed every 0.058 mm. Finally, the calibration error for the PIV camera is 0.058 pixel or 0.0003 mm which is negligible.

3.2.3 PIV velocity uncertainty

Particle slip

In the trough of the waves, the flow abruptly changes direction and acceleration can be as high as 1×10^4 m s^{-2}. However, the small inertia of the particles ensures a very quick response. The particle time constant, given in Adrian and Westerweel (2011), is:

$$\tau_p = \frac{(\rho_p - \rho_f)d_p^2}{18\rho_f v\phi} \tag{4}$$

ρ_p and ρ_f are the particle and fluid density, respectively, d_p is the particle diameter, v is the fluid kinematic viscosity and ϕ is a function which tends toward 1 for a Stokes flow. In the present case, $\tau_p = 6. \times 10^{-7}$ s, which gives a velocity slip of up to 6 mm s^{-1}. The slip due to gravity (settling velocity) is negligible because the gravitational acceleration is several orders of magnitude smaller than the local flow acceleration. Therefore the uncertainty, ϵ_{slip}, is up to 0.3 % in the troughs, where the local velocity is around 1.9 m s^{-1}.

PIV algorithm

From the synthetic images results, the uncertainty of the PIV algorithm is estimated to be $\epsilon_{algo,b} = 1.8 \%$ for the vectors non-adjacent to the surface and $\epsilon_{algo,s} = 2.9 \%$ for the near-surface velocities.

The errors due to the timing (repeatability of laser, stability of the delay/pulse generator) are negligible, once the laser is properly calibrated and monitored. The calibration error is also negligible. The total uncertainty on the velocity measured by the current method is dominated by ϵ_{algo}. It should be noted that some PIV frames have glare that can prevent the computation of the velocity in the vicinity of the surface and decrease the overall accuracy of the measurement. This can be solved using fluorescent particles (Bardet et al. 2010).

3.2.4 PIV vorticity uncertainty

Lourenco and Krothapalli (1995) derived an expression for the error in the measurement of vorticity. The error is composed of the truncation error associated with the finite difference scheme used to compute derivatives and an additional term due to the error on the velocity. The error due to truncation is of order δ^2 for a central difference scheme, while the error from velocity error goes with δ^{-1}, where δ is the vector grid spacing. Therefore, the error on the vorticity can be minimized with optimum grid spacing.

Table 3 shows the levels of vorticity fluctuation in the bulk measured for three different sizes of interrogation window with a 50 % overlap. The level of fluctuation increases when reducing the window size, which corresponds to the error associated with the velocity error ($\sim \delta^{-1}$). The truncation error which varies as δ^2 has no visible effect in this case and must be of smaller magnitude, probably due to the very small grid spacing. The 32×32 window has not been chosen, because it is too coarse to correctly capture the small flow structures present in this flow.

To estimate the error in vorticity, it is possible here to take advantage of the low velocity fluctuations in the bulk of the flow. A separate preliminary PIV measurement of

Table 3 Maximum deviation of the vorticity measured in the bulk for various interrogation window sizes and 50 % overlap

Window size (pixels)	δ (mm)	Vorticity fluctuations in bulk (s^{-1})
16×16	0.039	$\pm 8.6 \times 10^2$
24×24	0.058	$\pm 4.8 \times 10^2$
32×32	0.077	$\pm 2.7 \times 10^2$

the whole jet at lower magnification ($M = 0.4$) has been previously performed. This study was not time resolved, allowing for better optimization of the time interval between pulses for a given interrogation window size, following Adrian and Westerweel (2011). The focus was on the statistical characterization of jet velocity profile, not on the flow just below the surface. These favorable experimental conditions led to a better accuracy on the bulk velocity measurement, but at a lower spatial resolution (0.28 mm). The level of fluctuations was measured at 0.5 % of the bulk velocity. Because the interrogation window size remained small, it could be assumed that the error in vorticity is also dominated by the δ^{-1} term from the velocity.

Foucault and Stanislas (2002) developed expressions for the vorticity noise ϵ_{vort} based on the RMS of the velocity error $\epsilon_{velo,b}$. Equation 5 is for the current scheme (central difference).

$$\epsilon_{vort} = 0.71 \frac{\epsilon_{velo,b} U}{\delta} \tag{5}$$

By applying Eq. 5 to the low magnification PIV results, an upper limit for the bulk vorticity fluctuations is calculated to be 32 s^{-1}. This value is <10 % of the value reported in Table 3 for a 24 × 24 pixels window, which means that the tabulated value is mostly representing the error on the vorticity measurement and not on the actual flow fluctuations. When applying Eq. 5 to the high-magnification data reported here with $\epsilon_{velo,b} = 1.8$ %, $U = 2.36$ m s^{-1} and $\delta = 0.058$ mm, one obtains $\epsilon_{vort} = 5.2 \times 10^{2}$ s^{-1} which is in agreement with the value of 4.8×10^{2} s^{-1} reported in Table 3. The maximum amplitude of the measured vorticity being 4.0×10^{3} s^{-1} in the primary vortices core, the error on the bulk vorticity is 12 %.

4 Post-processing at the surface

The processing of the PLIF and PIV data provides the interface profile and the liquid velocity field below. The surface profile must be post-processed in order to improve the computation of slope and curvature. Velocity and vorticity are then calculated at the location of this post-processed interface allowing calculation of surface vorticity and vorticity flux.

4.1 Curve fit of the profile

Although the interface detection scheme gives a satisfactory surface profile for masking the PIV data, this profile must be further processed in order to compute the first and second derivatives. This methodology is not dissimilar to
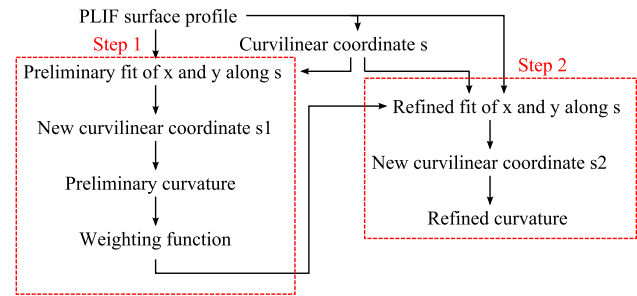
Fig. 12 Algorithm for computing the curvature from the PLIF profile

current practices in CFD. Because the PLIF profile is pixelized, the slope based on the direct neighboring pixels is discontinuous and cannot be computed in this manner.

While a low-pass spatial filter could be envisioned, it will reduce the magnitude of spatial derivatives, especially in regions of high curvature. A curve fitting is a better option, but a trade-off must be found between deviation from the original profile and smoothness. In particular, the crests have low curvature, and noise in the surface profile would results in large variation in the computed curvature. On the other hand, the troughs are significantly sharper and the fit must be closer in these regions to faithfully capture the true curvature.

A two-step iterative process is employed for the curve fit. The algorithm is presented in Fig. 12. To be robust for every type of profile, the surface profile, initially represented by a list of (x, y) coordinates, is converted to a parametric curve based on the curvilinear coordinate s. The curve is then described by the matrix $[s, x(s), y(s)]$. This method prevents ambiguities with multivalued functions, which can appear where the slope of the profile is equal to $\pm 90°$.

A preliminary spline curve is fitted to the profile, shown in Fig. 13a. A first estimate of the curvature, Fig. 13c, is computed using this curve and will serve as a weighting function, Eq. 6, for refining the fit in the second step. The exponent in Eq. 6 depends on how much emphasis is put on the trough, while the constant ensures that the low-curvature regions are still taken into account. Deviation from the PLIF profile for the preliminary and refined curve fits is shown in Fig. 13b. The curvilinear coordinate is updated for the refined profile, and the final curvature is calculated with Eq. 8 (discussed below), see Fig. 13c. With the refined fit, the deviation from the original profile is independent of the curvature and is below 0.012 mm (1.5 % of the profile amplitude or 2.5 pixels) with a root-mean-square (RMS) deviation of 0.6 % or 1 pixel. The refined calculation has improved the measurement of the high curvature in the troughs, without introducing noise in the regions of low curvature.
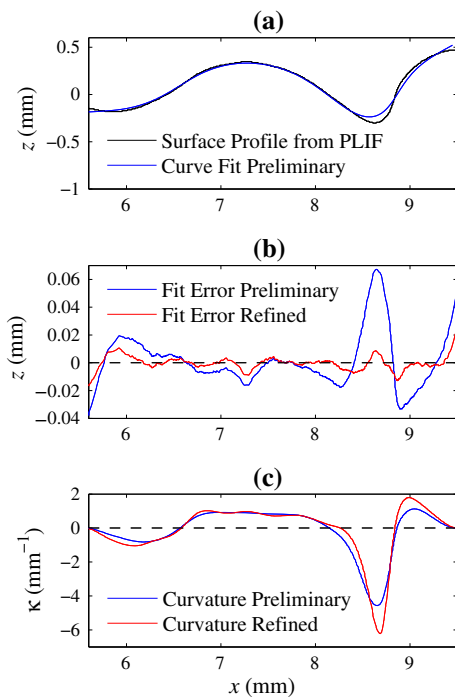
(a)

(b)

(c)

Fig. 13 **a** Comparison of the PLIF surface profile obtained in Sect. 3.1 with the preliminary curve fit. Fitting is poor in the trough. **b** Error in the fit for the preliminary fit and for the refined fit. The error is large in the trough for the preliminary fit, but is greatly improved for the refined fit. **c** Preliminary curvature used for weighting the refined fit and curvature from the refined fit. In the trough, accuracy is improved while no noise is introduced in the regions of low curvature. The refined profile is not shown, because it matches closely the PLIF profile and would not be distinguishable from it on (*a*)

Convergence with measured profile is sufficient, and a second iteration is not necessary.

$$\text{Weight} = \kappa^2 + \max(|\kappa|)/4 \qquad (6)$$

4.2 Curvature computation scheme

Curvature can be computed in several ways. The local curvature of the free surface can be defined based on the rate of change of the normal or tangent vectors:

$$\kappa_1 = \mathbf{s} \cdot \frac{\partial \mathbf{n}}{\partial s} = -\frac{\partial \mathbf{s}}{\partial s} \cdot \mathbf{n} \qquad (7)$$

A positive curvature corresponds to a convex surface, such as in Fig. 1. Alternatively the curvature of a parametric function can be calculated with Eq. 8, where the ′ denotes derivative with respect to *s*.

$$\kappa_2 = -\frac{x'y'' - y'x''}{(x'^2 + y'^2)^{3/2}} \qquad (8)$$

The curve fit of the surface profile with splines uses piecewise quadratic functions; hence, the curvature cannot

be calculated analytically with acceptable resolution. Instead, it is computed based on the parametric curve of the surface profile using a centered finite difference scheme. Furthermore, due to the projection from Cartesian to curvilinear coordinates, the points are not equally spaced along *s*, which must be accounted for when computing the derivatives. For instance, x' is calculated with the following finite difference scheme, Sfakianakis (2009):

$$h_i = s_i - s_{i-1} \qquad (9)$$

$$x'_i \approx \frac{h_i h_{i+1}}{h_i + h_{i+1}} \left(-\frac{x_{i-1}}{h_i^2} + \left(\frac{1}{h_i^2} - \frac{1}{h_{i+1}^2} \right) x_i + \frac{x_{i+1}}{h_{i+1}^2} \right) \qquad (10)$$

This scheme is of second order accuracy and uses 3 points. The second derivative can be computed similarly (Sfakianakis 2009):

$$x''_i \approx \frac{2}{h_i + h_{i+1}} \left(\frac{x_{i-1}}{h_i} - \left(\frac{1}{h_i} + \frac{1}{h_{i+1}} \right) x_i + \frac{x_{i+1}}{h_{i+1}} \right) \qquad (11)$$

This scheme is of first order accuracy and uses 3 points. A uniform grid would lead to a second order accuracy. Using the same schemes, the normal and tangent vectors in Eq. 7 are resolved at the second order while the vector derivatives are at the first order. Uncertainties in curvature are associated with curve fit goodness and finite difference computations. Relative influence of both effects is analyzed below.

To assess the resolution of the curvature computation, a family of Gaussian functions is used. The curvature at the peak is known analytically, and the overall profile is closer to waves than to circles traditionally used to evaluate interface tracking schemes in CFD, as done by François et al. (2006). Synthetic images of profile are generated based on Gaussian curves projected at various spatial resolution. Specifically, the relevant dimensionless parameter for this analysis is the peak radius of curvature $|\kappa|^{-1}$ normalized by the image resolution (or pixel side dimension) Δx and ranges between 2 and 700. It should be noted that a flat profile corresponds to $1/(|\kappa| \Delta x) \rightarrow +\infty$.

Figure 14 presents the uniform norm of the error in curvature L_∞ normalized by the maximum curvature, as a function of $1/(|\kappa| \Delta x)$. The maximum error is always located at the top of the Gaussian, where κ is maximum. It can be seen that the error is very similar for both schemes, although a small discrepancy is visible for $1/(|\kappa| \Delta x) < 10$. The error is around 12 % for a range of $1/(|\kappa| \Delta x)$ between 6 and 40. For $1/(|\kappa| \Delta x) > 40$, the curve fit matches well the original profile, i.e., the radius of curvature is well resolved. Both schemes have similar resolution and a power -1 trend is observed, which is consistent with the error being driven by the finite difference scheme at high image resolution. The effect of the two steps curve fitting is
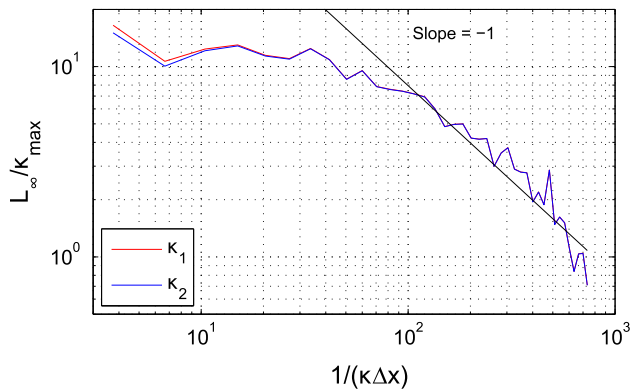
Fig. 14 Uniform norm of the error (in %) in curvature calculation for Eqs. 7 and 8

- ▬▬ Fitted surface profile
- - - - Stokes layer depth
- ● PIV datapoints
- ● Near-surface PIV datapoints
- ● Extrapolated datapoints
- ▪ Interpolated surface datapoints

Fig. 15 Surface quantities are based on extrapolation then interpolation of the PIV data

clearly visible for $1/(|\kappa|\Delta x) < 40$ where the error departs from the -1 trend.

These results are consistent with the work of Flynn and Jain (1989) on 3D curvature reconstruction, who found that it is difficult to get a curvature accuracy below 10 % for quantized data. An exception of this is for low values of curvature (with respect to spatial resolution), which can be resolved with higher accuracy.

The curvature scheme chosen is Eq. 8 because it has slightly better accuracy and curvilinear coordinates are readily available.

4.3 Surface velocity

Because of the finite size of the interrogation windows, PIV has an inherent limitation on spatial resolution. In the case of a free-surface flow, the shear stress at the surface in the liquid phase is zero. As the waves travel, an oscillatory boundary layer is created at the free surface (Longuet-Higgins 1992). This layer is of the order of the Stokes boundary layer (Schlichting and Gersten 2000) and depends on the radian frequency of the waves, Ω.

$$d = \sqrt{\frac{2\nu}{\Omega}} \qquad (12)$$

For 2 mm wavelength capillaries, the phase velocity is around 0.5 m s^{-1}. This results in a radian frequency of 1.5 $\times 10^3$ rad s^{-1} and a Stokes layer of 0.04 mm. In the present case, the high resolution results in surface adjacent vectors that are between 0 and 58 μm away from the interface. The expected error on the surface location is 18 μm (13 μm from the PLIF profile detection and 12 μm from the curve fitting).

Due to spatial averaging associated with PIV processing, the measured velocity near the surface is closely related to the velocity in the Stokes layer. Variations are expected based on the distance from the window center to the surface and local velocity gradients. Nevertheless, near-
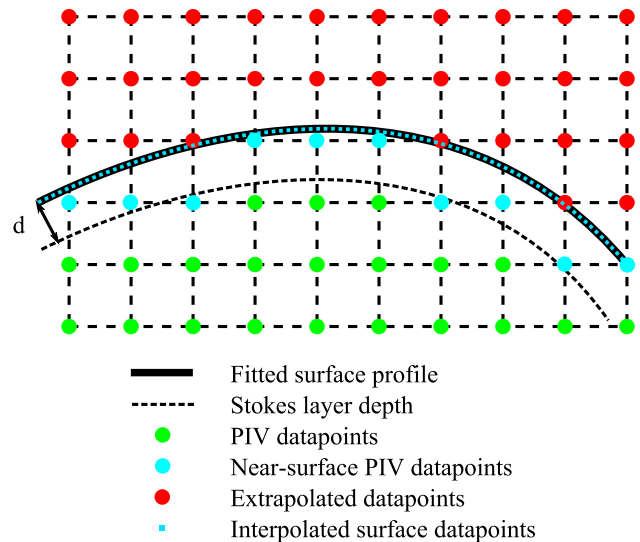
surface data (shown as large cyan dots in Fig. 15) provide a first estimate of the velocity and vorticity at the surface location. Velocity and vorticity at the surface location can then be resolved with reasonable confidence using the following extrapolation/interpolation scheme.

The raw PIV data (large green and cyan dots in Fig. 15) are extrapolated across the surface by iteratively taking the average of the nonzero neighboring datapoints, as shown in red in Fig. 15. The surface datapoints—represented by small cyan dots in Fig. 15—are then calculated at the location of the fitted profile for each curvilinear coordinate using cubic interpolation. For reference, the scale of the Stokes layer is shown with a dashed line in Fig. 15. Sample results are presented in the next section and illustrate the ability of this scheme to correct spatial variations due to the PIV grid, which is needed for computing spatial derivatives at the surface. The interpolated surface data are plotted along the near-surface raw PIV data in Figs. 19 and 21 for visualizing the result of the procedure described above.

4.4 Surface vorticity

Vorticity at the free surface can be obtained from the PIV vorticity data as explained in the previous section. Alternatively, the vorticity boundary condition, Eq. 1, derived from the shear-free condition on the liquid side of the interface can be used. In the present coordinate system and curvature definition, its expression is given by Eq. 13:

$$\omega_{n=0} = 2\frac{\partial u_n}{\partial s} - 2u_s\kappa \qquad (13)$$

Each method for obtaining the surface vorticity is subjected to uncertainties coming from different sources. The

uncertainty on vorticity from the PIV data has been estimated in Sect. 3.2.1 using synthetic images of a vortex. The error for the vorticity at the surface is 6.2 % where the vorticity is low and peaks up to 25 % in regions of high vorticity. A conservative estimation of the error based on synthetic results is defined in Eq. 14:

$$\epsilon_{\omega_{PIV}} = \max(0.25\omega_{n=0}, 0.062\max(\omega_{n=0})) \quad (14)$$

The error on the vorticity calculated with Eq. 13 is estimated using propagation of uncertainties. Its expression is given by Eq. 15 where ϵ_u and ϵ_k are the relative error in surface velocity and curvature, respectively. ϵ_u has been estimated to 2.9 % using synthetic data and ϵ_k is about 12 % based on the results of Sect. 4.2, with $1/(|\kappa|\Delta x) > 10$ in the present study. Although the derivative in Eq. 13 uses curvilinear coordinates, the uncertainty on this term must be calculated using the original vector spacing δ because the velocity has been interpolated along the surface profile.

$$\epsilon_{\omega_{Eq.13}} = 2\sqrt{\left(\frac{0.71 u_n \epsilon_u}{\delta}\right)^2 + (\kappa u_s \epsilon_u)^2 + (u_s \kappa \epsilon_\kappa)^2} \quad (15)$$

5 Experimental results

The flow under study exhibits various regimes. The boundary layer first relaxes while the free surface remains flat. Then for $Re_\theta > 150$, the shear layer rolls up into 2D spanwise vortices. Depending on the vortex velocity, the free surface can undergo large deformations, which remain 2D for the data presented here. This 2D canonical flow has been the subject of theoretical work on surface instability and generation of vorticity at a free surface. It is therefore well suited for validating the present experimental method.

Partial results of the flow regimes are shown below to demonstrate the diagnostics applicabilities to steep millimeter-scale waves.

5.1 Flat free surface

The high spatial resolution PIV allows resolving the boundary layer inside the nozzle and just after the exit. This allows characterizing the initial conditions, which is of particular importance to enabling the use of these datasets to validate high-fidelity CFD interface tracking methods.

Data for $U = 1.44$ m s^{-1} and $Re_\theta = 143$ are reported first. In this case, the flow is unidirectional, and the free surface remains nearly flat upon exiting the nozzle. The slower bulk velocity results in a thicker laminar boundary layer, which eases its experimental characterization. The PIV interrogation windows are decreased to 16×16 pixels with 50 % overlap. Since the flow is unidirectional, the interrogation windows are stretched in the flow direction by a ratio 4:1 to refine the measurement of the shear-layer profile. The resulting vector spacing is 0.039 mm. Data are acquired at three different locations (centered on $x = -2$, 2 and 8 mm) and averaged over 2,000 frames. Four averaged velocity profiles have been extracted from these fields and are plotted on the left of Fig. 16. Since the jet thickness decreases by about 0.5 % to satisfy mass conservation due to acceleration of the boundary layer at the free surface, data are reported with respect to the local surface elevation, which is set at $z = 0$. The RMS of the fluctuations are also reported on the right of Fig. 16. The measured bulk fluctuations (1.2 %) are within the error of the current method (1.8 %), the actual value is closer to 0.5 %, see Sect. 3.2.4.
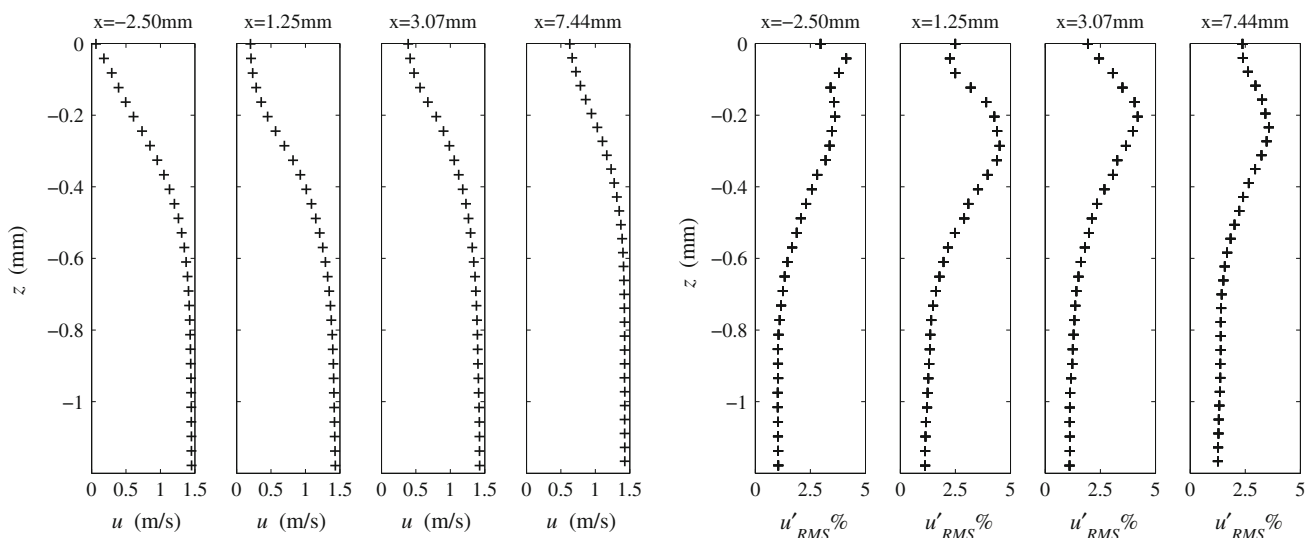

Fig. 16 $U = 1.44$ m s^{-1}. $Re_\theta = 143$. *Left* Velocity profiles near the top of the layer at four different locations. $z = 0$ corresponds to the free-surface elevation. *Right* RMS of the velocity fluctuations for the respective profiles. Measured bulk fluctuations are 1.2 % of U
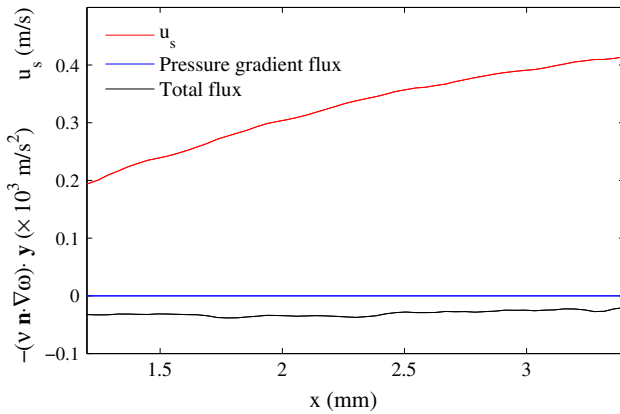
Fig. 17 Free-surface tangent velocity and vorticity flux as a function of the downstream location for the data presented Fig. 16

The velocity fluctuations increase in the shear layer to about 4 % of the bulk velocity.

More than 12 datapoints are resolved in the shear layer. The shear-free region just below the interface is ~ 0.04 mm, which is similar to the thickness of the Stokes layer. The measured wall shear stress before the relaxation is 2.9 Pa, while the model used for designing the nozzle (Thwaites' method, see André and Bardet 2012) predicts a value of 3.4 Pa. The measured shear stress at the surface ($x \geq 0$, $z = 0$) is between 0.1 and 0.8 Pa, which is close to a shear-free condition. The small discrepancy may be due to the stress induced by the gas phase, which tends to oppose the acceleration of the surface, but are mostly driven by the limited resolution of the measurement of surface velocity. The free-surface acceleration is clearly captured; the surface speed recovers more than 50 % of the bulk velocity over the first 10 mm after the nozzle exit.

The acceleration of the free surface represents a flux of vorticity through the surface. The expression for the vorticity flux derived in "Appendix 3" in the case of a flat steady free surface simplifies to Eq. 16. It is worth noting that the pressure gradient term is still present in this case (second term in the right hand side).

$$-(v\mathbf{n} \cdot \nabla \omega) \cdot \mathbf{y} = -\left(\frac{1}{2} \frac{\partial (u_s^2)}{\partial s} - 2v \frac{\partial^2 u_s}{\partial s^2} \right) \quad (16)$$

Figure 17 shows the surface velocity along with results for the flux. The magnitude of the pressure gradient term is on the order of 10^{-3} m s^{-2} and is therefore negligible compared to the advective acceleration term (3×10^1 m s^{-2}). The total flux is negative and nearly constant at -3×10^1 m s^{-2}. This signifies that the flow gives out positive vorticity. The change in net flux given by Eq. 17 is related to the change in advected vorticity inside the flow (Dabiri and Gharib 1997), Eq. 18. In this unidirectional case, they are equal since the pressure gradient term is negligible.

A comparison of the computed values will therefore lead to identical results.

$$\zeta = -\int_{x_1}^{x_2} v(\mathbf{n} \cdot \nabla \omega) \cdot \mathbf{y} ds \simeq \frac{1}{2}\left(u_s(x_1)^2 - u_s(x_2)^2 \right) \quad (17)$$

$$\int_{-\infty}^{0} u(x_2, z)\omega dz - \int_{-\infty}^{0} u(x_1, z)\omega dz = \frac{1}{2}\left(u_s(x_1)^2 - u_s(x_2)^2 \right) \quad (18)$$

5.2 Shear layer roll-up

Figure 18 shows the roll-up of the shear-layer downstream of the nozzle for $U = 2.36$ m s^{-1} and $Re_\theta = 177$. Discrete vortices with a spacing of 1.9 mm are identifiable. The occurrence and location of a vortex can be found with several criteria (Adrian et al. 2000a, b); here, it is based on the swirling strength (Zhou et al. 1999). In this case, the vortices are traveling at 1.8 m s^{-1}.

The dimensionless frequency of the instability is calculated using Eq. 3. In the present case, with $f = U_{vortex}/\lambda$, $\theta = 0.075$ mm and $U = 2.36$ m s^{-1}, $\bar{f} = 0.19$, which is in agreement with Brennen's result.

The average circulation per wavelength Γ_λ, measured by integrating the vorticity from the PIV data is 2.3×10^{-3} m^2/s. The initial circulation in the boundary layer at the nozzle exit for a length equivalent to one wavelength is simply $\Gamma_{x=0} = U\lambda = 4.5 \times 10^3$ m^2 s^{-1}. The difference corresponds to what has fluxed out between the exit and this particular downstream location. Using a flat free-surface approximation, the difference is $\Gamma_{x=7.5mm} = (U - u_s)\lambda = 2.4 \times 10^{-3}$ m^2/s where $u_s = 1.1$ m s^{-1} is the surface velocity at this downstream location. $\Gamma_{x=0} - \Gamma_{x=7.5mm} = 2.1 \times 10^{-3}$ m^2 s^{-1}, which is within 10 % of Γ_λ. This circulation budget confirms the high vorticity magnitude visible in the PIV data. Such high values are a consequence of the small temporal and spatial scales of the flow. Furthermore, the vortices are resolved with more than 12 velocity vectors and stay coherent within each PIV frame in the time series. Additionally, for this particular surface profile, the local angle of incidence of the laser sheet with respect to the surface slope is significantly below the Brewster angle and light reflection at the water-air surface can be neglected, see Sect. 3.1.1.

Figure 19 shows the surface vorticity corresponding to Fig. 18 computed with schemes introduced earlier. Surface vorticity interpolated from the PIV data is plotted as a thick red line. The thinner red lines represent the uncertainty at 95 % confidence on this measurement calculated with Eq. 14.

The vorticity at the near-surface PIV datapoints is reported as red crosses. As shown in Fig. 15, these points

Fig. 18 PIV vector field with vorticity color plot and streamlines. $U = 2.36$ m s^{-1}. $Re_\theta = 177$. Vortex velocity ($U_{vortex} = 1.8$ m s^{-1}) has been subtracted. All vectors are displayed. The streamlines are plotted to show the roll-up of the shear layer in discrete vortices
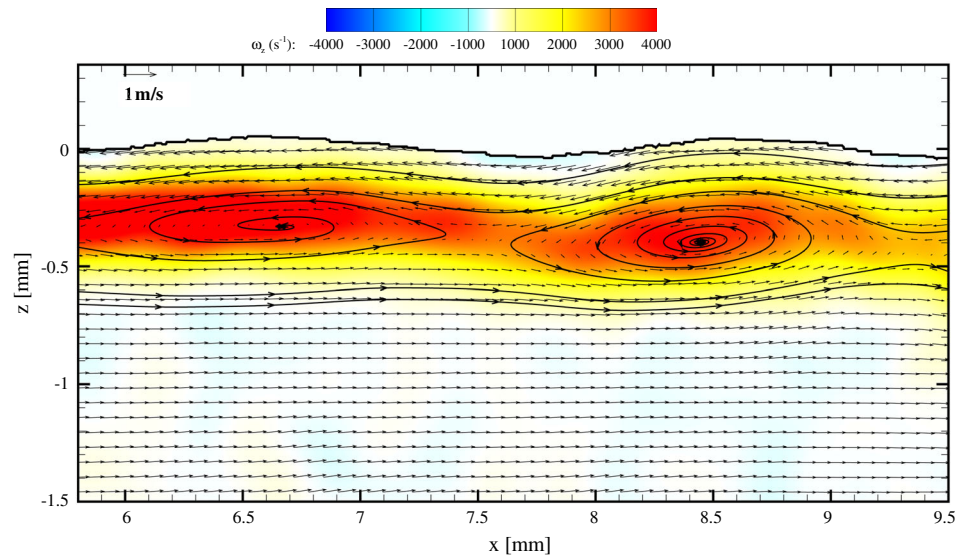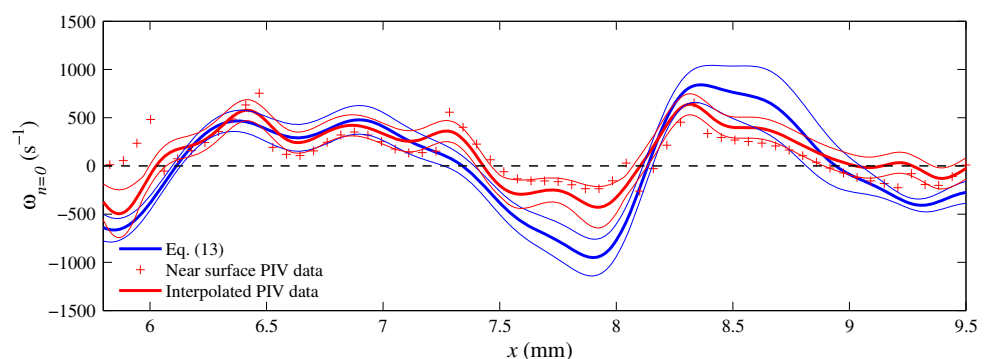

Fig. 19 Comparison of the surface vorticity from the PIV data versus Eq. 13 for Fig. 18. The *thick red line* is the vorticity interpolated at the surface location. The crosses are the near-surface raw PIV data. The *thinner lines* show the uncertainty at 95 % confidence for each measurement

are within or very close to the Stokes layer. The surface vorticity from PIV data exhibits jumps, such as at $x = 6$ mm or $x = 7.25$ mm. This is attributed to the PIV grid; the actual distance of adjacent datapoints to the true interface varies by multiples of the grid spacing, as illustrated in Fig. 15. This nonuniform spacing leads to significant variations in vorticity, see discussion in Sect. 4.3. Other variations are discussed in Sect. 5.3.

The thick blue line is the surface vorticity calculated with Eq. 13. Similarly, the thin blue lines show the corresponding uncertainty calculated with Eq. 15.

The curves follow a very similar trend and are in agreement within the associated uncertainties, which confirms the possibility of resolving velocity and vorticity at a free surface. Finally, negative vorticity is visible in the vicinity of the trough, which is consistent with diffusion of vorticity highlighted by Longuet-Higgins (1992).

5.3 Large amplitude waves

A PIV vector field with vorticity color plot and streamlines under large amplitude waves, corresponding to the profile Fig. 13, is presented in Fig. 20. The corresponding surface vorticity is shown in Fig. 21. Note that in this case, the location of maximum swirling strength does not coincide exactly with the location of maximum vorticity. The flow regime is the same as in the previous sub-section; however, the growth of the waves is larger, probably because the shear layer has rolled up at a different depth. The distance between the two vortices is now 2.45 mm. The dimensionless frequency is $\bar{f} = 0.16$, which is still consistent with Brennen's results.

Vortices also have a similar strength to those in Fig. 18. The wave on the left has a small streamwise slope, and hence, the velocity field below that wave can be resolved with PIV with high accuracy. The wave on the right, however, has a steep streamwise slope and the laser sheet angle of incidence with respect to the wave exceeds the critical total internal reflection angle. Furthermore, the surface curvature results in a focused laser beamlet that is redirected in the flow. Hence, in the raw PIV data, the local SNR is lower than in other segments of the frame, see discussion in Sect. 3.1.1. In this particular velocity field, this corresponds to the top of the vortex below the wave. It should be noted, however, that the lower part of the vortex is unaffected by this phenomenon. Despite this change in

Fig. 20 PIV vector field with vorticity contour plot. $U = 2.36$ m s^{-1}. $Re_\theta = 177$. Vortex velocity ($U_{vortex} = 2.0$ m s^{-1}) has been subtracted. All vectors are displayed. Generation of negative vorticity can be seen around $x = 8.6$ mm. This frame corresponds to the surface profile of Fig. 13
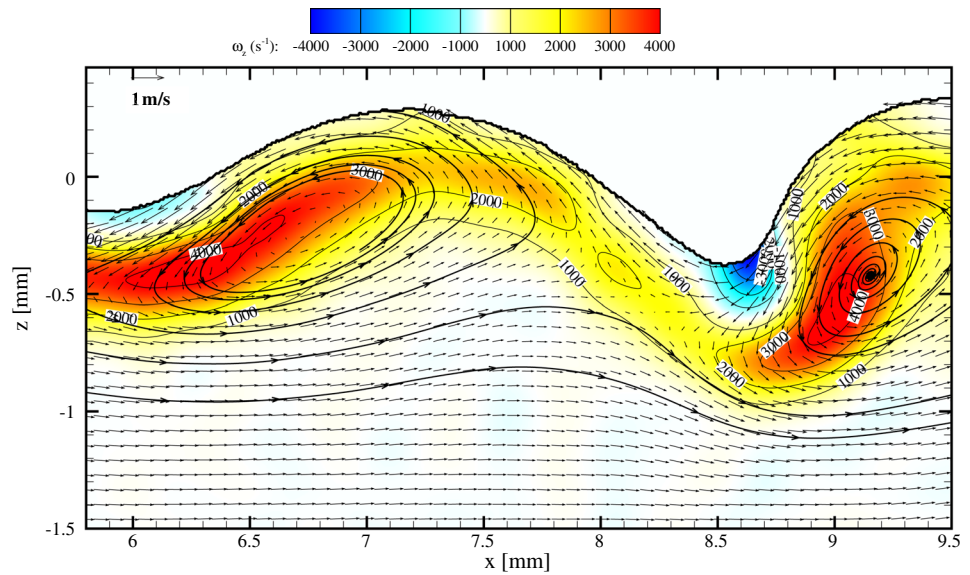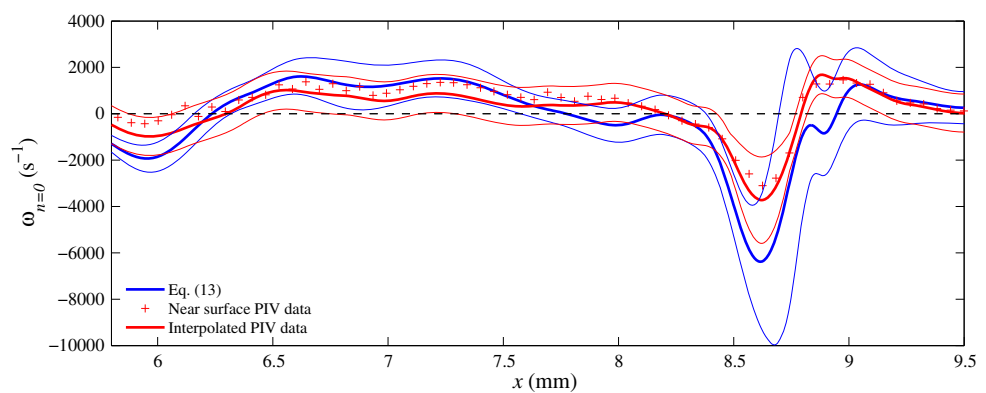

Fig. 21 Comparison of the surface vorticity from the PIV data versus Eq. 13 for Fig. 20. The *thick red line* is the vorticity interpolated at the surface location. The crosses are the near-surface raw PIV data. The *thinner lines* show the uncertainty at 95 % of confidence for each measurement

SNR across this flow feature, the velocity field and vorticity magnitude stay spatially coherent. Furthermore, the growth of this wave was tracked temporally. Initially, the wave was similar to the left wave, and the vortex kept its coherence and magnitude through the transient evolution. This confirms that spatial and temporal coherences of the flow are well captured by the diagnostics.

High magnitude negative vorticity is present in the trough of the wave. This vorticity is generated by the moving curved free surface and allows comparing the accuracy of the measurement against Eq. 13 (through Fig. 21) as done in the previous subsection. Variations in vorticity from near-surface PIV data (red crosses) are also slightly visible around such instance as $x = 6.5$ mm. The larger vorticity magnitude makes these variations less pronounced. In this figure, the curves are also in agreement with each other. The largest discrepancies are in regions where the surface vorticity has a high magnitude, as could be expected from the synthetic data. This shows that the high spatial resolution (about 6 velocity vectors are produced in the sharpest part of

the trough) of the present method can capture surface vorticity to some accuracy. In particular, the negative vorticity measured in the bulk that was generated at the surface is consistent in magnitude with values of surface vorticity within their uncertainties ($-6,500$ s^{-1} at the surface and $-4,000$ s^{-1} in the fluid).

It is also worth noting that both terms of Eq. 13 have a much larger magnitude than the resulting surface vorticity. They are plotted in Fig. 22 for the surface vorticity presented Fig. 21. They have opposite sign and cancel most of each other out when summed. This can be related to the large velocity at which the surface is traveling in the laboratory frame of reference. The curvature term is positive in this frame of reference, but becomes negative when measured in the frame of reference moving with the wave. This is illustrated in Fig. 20, where the vortex velocity (approximately equal to the wave velocity) has been subtracted. It can be seen in this figure that in the trough, $u_s < 0$, $\kappa < 0$ and therefore $-2u_s\kappa < 0$. The term $2\frac{\partial u_n}{\partial s}$ changes accordingly, as the vorticity is the same in any Galilean frame of reference.
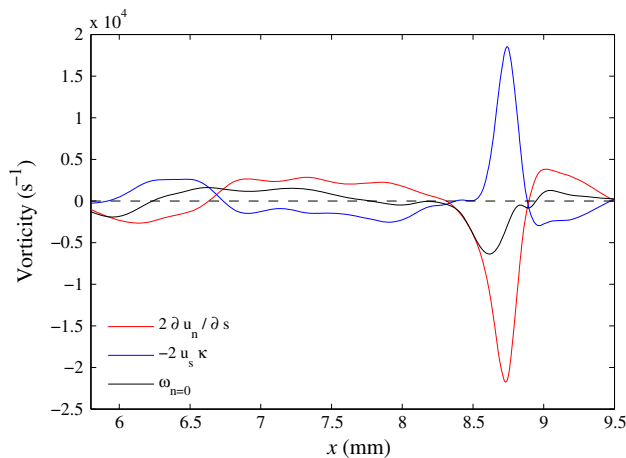
Fig. 22 Decomposition of the terms of the surface vorticity, Eq. 13 for the data of Fig. 21

6 Conclusions

The present method takes advantage of recent progress in high-speed cameras and lasers to address common diagnostics limitations in liquid/gas interface in multiphase flows. One challenge is characterizing the interface profile to use it for the PIV processing where the surface is not readily identifiable. The surface profile is accurately determined with PLIF, and PIV provides velocity and vorticity data very close to the surface. It is thus possible to measure the surface vorticity with the PIV vorticity field, or with surface velocity and curvature. It has been shown that both approaches are in agreement. This diagnostic is applied to shear layer-instability below the surface of a high-speed water wall jet. High-spatio-temporal resolution is obtained: 58 μm and 62.5 μs. The spatial resolution is on the order of the Stokes layer depth below the surface. The system allows resolving for the first time subsurface velocity field below high amplitude millimeter-scale waves ($\lambda \sim 2$ mm, $ak > 2$, and nearly vertical slopes). Detailed data are obtained on the roll-up of the shear layer, growth mechanism of surface disturbances, and vorticity generation. Such data are also useful for validating high-fidelity multiphase CFD codes. The method can be adapted to other types of free-surface flows provided that there is optical access to the top and bottom of the surface for PLIF and PIV, respectively.

Appendix 1

In order to find the relation between γ_1, γ_2, and g/w, a spherical coordinate system is used to represent all the possible spanwise and streamwise angles. ϕ and ψ are respectively the polar and azimuthal angles of the spherical coordinate system shown in Fig. 23.

$\mathbf{v}$ is the unit vector pointing toward the PLIF camera and $\mathbf{n}$ is the local surface normal unit vector. γ_1 is defined as the angle between the axis $\mathbf{z}$ and the projection of $\mathbf{n}$ in the plane containing $\mathbf{x}$ and $\mathbf{z}$, and its expression is given by Eq. 19:

$$\gamma_1 = \arctan(\sin(\phi)\tan(\psi)) \tag{19}$$

γ_2 is defined as the angle between the axis $\mathbf{y}$ and $\mathbf{n}$, minus $\pi/2$, and its expression is given by Eq. 20:

$$\gamma_2 = \arcsin(\sin(\psi)\cos(\phi)) \tag{20}$$

The apparent thickness of the gradient zone, as seen by the camera is given by Eq. 21:

$$g = \frac{w}{\cos(\gamma_2)}\mathbf{v} \cdot \mathbf{n} \tag{21}$$

which can be rewritten

$$\frac{g}{w} = \frac{\cos(\alpha_2)\cos(\phi)\sin(\psi) + \sin(\alpha_2)\cos(\psi)}{\cos(\gamma_2)} \tag{22}$$

By plugging Eq. 20 into 22, the system reduces to a second degree polynomial function whose variable is $\cos(\phi)$ and whose coefficients depend on g/w and ψ. Once ψ and ϕ are known for a given g/w, γ_1 and γ_2 can be calculated a posteriori. Direct calculation of γ_2 from γ_1 and g/w can be done graphically using Fig. 8 or requires an iterative process.
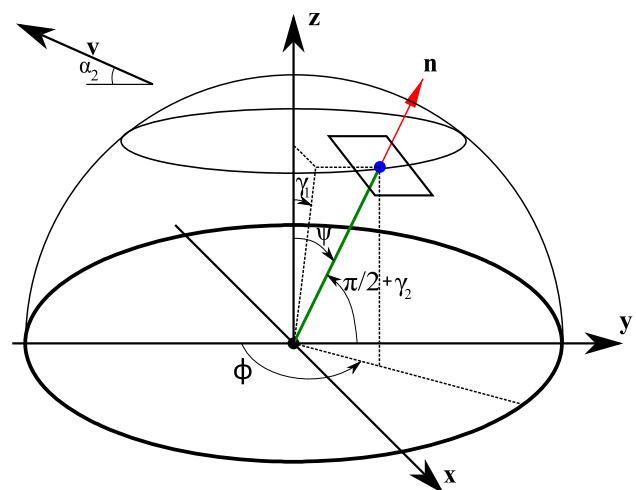

Fig. 23 Spherical coordinate system. $\mathbf{v}$ is the viewing vector pointing toward the PLIF camera

Appendix 2

The surface profile can be approximated in the spanwise direction by a second order Taylor expansion:

$$f\left(x, y + \frac{w}{2}\right) = f(x, y) + \frac{w}{2}\tan(\gamma_2)$$
$$+ \frac{w^2}{8}\kappa_y\left(1 + (\tan(\gamma_2))^2\right)^{3/2} + O(w^3)$$

(23)

The change in elevation due to the spanwise curvature, κ_y, can be estimated using the second order term of Eq. 23. The error due to this term, ϵ_y is plotted in Fig. 24. Additionally, curvature can limit the angle at which the spanwise profile can be entirely seen. The limit is given by Eq. 24, and the region above this limit is shown in gray in Fig. 24.

$$|\kappa_y| = \frac{4(\tan(\alpha_2) + \tan(\gamma_2))}{w\left(1 + (\tan(\gamma_2))^2\right)^{3/2}}$$

(24)

Appendix 3

In the present coordinate system for a 2D flow, the flux of surface parallel vorticity through the surface is given by Eq. 25 (Rood 1995; Gharib and Weigand 1996). Note that the out of plane vector $\mathbf{s} \times \mathbf{n}$ is $-\mathbf{y}$ by consistency with the coordinate system defined in Figs. 1 and 2.

$$v\mathbf{n} \cdot \nabla\omega = \left(\frac{\partial u_s}{\partial t} - u_n\omega_{n=0} + \frac{1}{2}\frac{\partial(u_s^2 + u_n^2)}{\partial s} + \frac{1}{\rho}\frac{\partial p}{\partial s} - g\sin\gamma_1\right)\mathbf{y}$$

(25)

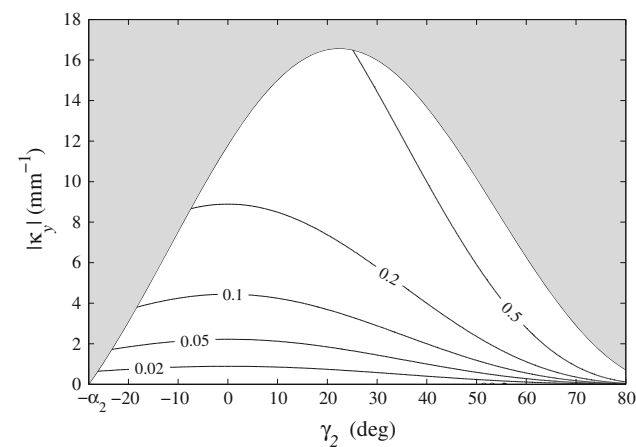**Fig. 24** Iso-contour of ϵ_y/w (in %) showing the error in the surface elevation induced by neglecting the second order term (spanwise surface curvature). Region where the interface is masked due to the curvature is in *gray*

The pressure gradient term can be obtained based on the surface normal stress boundary condition (Lundgren and Koumoutsakos 1999):

$$p = p_{\text{gas}} + \sigma\kappa - 2\mu\left(\frac{\partial u_s}{\partial s} + u_n\kappa\right),$$

(26)

where p_{gas} is the pressure on the gas side of the interface, which can be assumed constant.

The five terms contributing to the flux are surface acceleration, advected surface vorticity, advective acceleration, pressure gradient and gravity, in the same order as they appear in the right hand side of Eq. 25. According to Dabiri and Gharib (1997), the net vorticity flux through the surface ζ, can be calculated with the running integral of Eq. 25 with respect to s as following:

$$\zeta = -\int_{s_0}^{s} v(\mathbf{n} \cdot \nabla\omega) \cdot \mathbf{y}\,\mathrm{d}s$$

(27)

It should be noted that a flux of positive vorticity into the liquid and a flux of negative vorticity out of the liquid will both result in $-(v\mathbf{n} \cdot \nabla\omega) \cdot \mathbf{y} > 0$. The temporal evolution of the bulk vorticity can be used to solve this ambiguity.

References

Adrian R (1988) Double exposure, multiple-field particle image velocimetry for turbulent probability density. Opt Lasers Eng 9(3):211–228

Adrian R (1997) Dynamic ranges of velocity and spatial resolution of particle image velocimetry. Meas Sci Technol 8(12):1393

Adrian R, Westerweel J (2011) Particle image velocimetry. Cambridge University Press, Cambridge

Adrian R, Christensen K, Liu ZC (2000a) Analysis and interpretation of instantaneous turbulent velocity fields. Exp Fluids 29(3):275–290

Adrian R, Meinhart C, Tomkins C (2000b) Vortex organization in the outer region of the turbulent boundary layer. J Fluid Mech 422(1):1–54

André M, Bardet P (2012) Experimental investigation of boundary layer instabilities on the free surface of non-turbulent jet. In: Proceedings of the ASME fluids engineering division summer meeting

Banner ML, Peirson WL (1998) Tangential stress beneath wind-driven air–water interfaces. J Fluid Mech 364(115–145):21

Bardet P, Peterson P, Savaş O (2010) Split-screen single-camera stereoscopic piv application to a turbulent confined swirling layer with free surface. Exp Fluids 49:513–524

Bardet P, André M, Neal D (2013) Systematic timing errors in laser-based transit-time velocimetry. In: 10th International symposium on particle image velocimetry-PIV13 (in press)

Barnhart DH, Adrian RJ, Papen GC (1994) Phase-conjugate holographic system for high-resolution particle-image velocimetry. Appl Opt 33(30):7159–7170

Batchelor GK (1967) An introduction to fluid mechanics. Cambridge University Press, Cambridge

Belden J, Techet AH (2011) Simultaneous quantitative flow measurement using piv on both sides of the air–water interface for breaking waves. Exp Fluids 50(1):149–161

Bitter M, Scharnowski S, Hain R, Kähler CJ (2011) High-repetition-rate piv investigations on a generic rocket model in sub-and supersonic flows. Exp Fluids 50(4):1019–1030

Brennen C (1970) Cavity surface wave patterns and general appearance. J Fluid Mech 44:33–49

Bryanston-Cross P, Epstein A (1990) The application of sub-micron particle visualisation for piv (particle image velocimetry) at transonic and supersonic speeds. Prog Aerosp Sci 27(3):237–265

Crimaldi J (2008) Planar laser induced fluorescence in aqueous flows. Exp Fluids 44(6):851–863

Dabiri D, Gharib M (1997) Experimental investigation of the vorticity generation within a spilling water wave. J Fluid Mech 330:113–139

Dabiri D, Gharib M (2001) Simultaneous free-surface deformation and near-surface velocity measurements. Exp Fluids 30(4):381–390

Duchon CE (1979) Lanczos filtering in one and two dimensions. J Appl Meteorol 18(8):1016–1022

Duncan JH, Qiao H, Philomin V, Wenz A (1999) Gentle spilling breakers: crest profile evolution. J Fluid Mech 379:191–222

Elsinga G, Scarano F, Wieneke B, Van Oudheusden B (2006) Tomographic particle image velocimetry. Exp Fluids 41(6):933–947

Flynn PJ, Jain AK (1989) On reliable curvature estimation. In: Proc IEEE Conf Computer Vision and Pattern Recognition, vol 89, pp 110–116

Foeth E, van Doorne C, van Terwisga T, Wieneke B (2006) Time resolved PIV and flow visualization of 3D sheet cavitation. Exp Fluids 40(4):503–513

Foucaut J, Stanislas M (2002) Some considerations on the accuracy and frequency response of some derivative filters applied to particle image velocimetry vector fields. Meas Sci Technol 13(7):1058

François MM, Cummins SJ, Dendy ED, Kothe DB, Sicilian JM, Williams MW (2006) A balanced-force algorithm for continuous and sharp interfacial surface tension models within a volume tracking framework. J Comput Phys 213(1):141–173

Gharib M, Weigand A (1996) Experimental studies of vortex disconnection and connection at a free surface. J Fluid Mech 321:59–86

Henderson F (1966) Open channel flow. Macmillan series in civil engineering, Macmillan. http://books.google.com/books?id=4whSAAAAMAAJ

Hirsa A, Vogel M, Gayton J (2001) Digital particle velocimetry technique for free-surface boundary layer measurements: application to vortex pair interactions. Exp Fluids 31:127–139

Kuang-An C, Liu LF (1998) Velocity, acceleration and vorticity under a breaking wave. Phys Fluids 10(1):29–44

Law C, Khoo B, Chew T (1999) Turbulence structure in the immediate vicinity of the shear-free air–water interface induced by a deeply submerged jet. Exp Fluids 27(4):321–331

Li FC, Kawaguchi Y, Segawa T, Suga K (2005) Wave-turbulence interaction of a low-speed plane liquid wall-jet investigated by particle image velocimetry. Phys Fluids 17(082):101

Lin H, Perlin M (1998) Improved methods for thin, surface boundary layer investigations. Exp Fluids 25(5–6):431–444

Lin H, Perlin M (2001) The velocity and vorticity fields beneath gravity-capillary waves exhibiting parasitic ripples. Wave Motion 33(3):245–257

Lin J, Rockwell D (1995) Evolution of a quasi-steady breaking wave. J Fluid Mech 302(1):29–44

Longuet-Higgins M (1992) Capillary rollers and bores. J Fluid Mech 240:659–679

Longuet-Higgins M (1994) Shear instability in spilling breakers. Proc R Soc Math Phys Sci 446:399–409

Lourenco L, Krothapalli A (1995) On the accuracy of velocity and vorticity measurements with PIV. Exp Fluids 18(6):421–428. doi:10.1007/BF00208464

Lugt HJ (1987) Local flow properties at a viscous free surface. Phys Fluids 30:3647

Lundgren T, Koumoutsakos P (1999) On the generation of vorticity at a free surface. J Fluid Mech 382(1):351–366

Meinhart C, Wereley S, Santiago J (1999) PIV measurements of a microchannel flow. Exp Fluids 27(5):414–419

Otsu N (1975) A threshold selection method from gray-level histograms. Automatica 11(285–296):23–27

Peirson W (1997) Measurement of surface velocities and shears at a wavy air–water interface using particle image velocimetry. Exp Fluids 23:427–437

Perlin M, He J, Bernal LP (1996) An experimental study of deep water plunging breakers. Phys Fluids 8:2365–2374

Phan T, Nguyen C, Wells J (2005) A PIV processing technique for directly measuring surface-normal velocity gradient at a free surface. ASME, New York City

Prasad AK (2000) Stereoscopic particle image velocimetry. Exp Fluids 29(2):103–116

Qiao H, Duncan J (2001) Gentle spilling breakers: crest flow-field evolution. J Fluid Mech 439(1):57–85

Raffel M, Willert C, Kompenhans J (1998) Particle image velocimetry: a practical guide. Exp Fluid Mech Ser, Springer-Verlag GmbH, http://books.google.com/books?id=dopRAAAAMAAJ

Rood EP (1995) Vorticity interactions with a free surface. In: Green SI (ed) Fluid vortices. Kluwer in Dordrecht, The Netherlands, pp 687–730

Saffman P (1993) Vortex dynamics. Cambridge University Press, Cambridge

Santiago J, Wereley S, Meinhart C, Beebe D, Adrian R (1998) A particle image velocimetry system for microfluidics. Exp Fluids 25(4):316–319

Scarano F, Riethmuller M (2000) Advances in iterative multigrid piv image processing. Exp Fluids 29(1):S051–S060

Scardovelli R, Zaleski S (1999) Direct numerical simulation of free-surface and interfacial flow. Ann Rev Fluid Mech 31(1):567–603

Schlichting H, Gersten K (2000) Boundary-layer theory. Springer, Berlin

Sfakianakis N (2009) Finite difference schemes on non-uniform meshes for hyperbolic conservation laws. Ph.D. thesis, University of Crete, Heraklion

Siddiqui MK, Loewen MR, Richardson C, Asher WE, Jessup AT (2001) Simultaneous particle image velocimetry and infrared imagery of microscale breaking waves. Phys Fluids 13:1891

Theunissen R, Scarano F, Riethmuller M (2008) On improvement of PIV image interrogation near stationary interfaces. Exp fluids 45(4):557–572

Tsuei L, Savaş Ö (2000) Treatment of interfaces in particle image velocimetry. Exp Fluids 29(3):203–214

Westerweel J, Hofmann T, Fukushima C, Hunt J (2002) The turbulent/non turbulent interface at the outer boundary of a self-similar jet. Exp Fluids 33:873–878

Wiederseiner S, Andreini N, Epely-Chauvin G, Ancey C (2011) Refractive-index and density matching in concentrated particle suspensions: a review. Exp Fluids 50(5):1183–1206

Yu D, Tryggvason G (1990) The free-surface signature of unsteady, two-dimensional vortex flows. J Fluid Mech 218:547–572

Zhou J, Adrian R, Balachandar S, Kendall T (1999) Mechanisms for generating coherent packets of hairpin vortices in channel flow. J Fluid Mech 387:353–396